Improved partially saturated method for the lattice Boltzmann pseudopotential multicomponent flows

Gang Wang, Umberto d'Ortona, Pierrette Guichardon

An improved partially saturated method for the lattice Boltzmann pseudopotential multicomponent flows

Gang Wang,* Umberto D'Ortona, and Pierrette Guichardon
Aix-Marseille Univ., CNRS, Centrale Marseille, M2P2, Marseille, France
(Dated: November 26, 2023)

This paper extends the partially saturated method (PSM), used for curved or complex walls, to the lattice Boltzmann (LB) pseudopotential multicomponent (MC) model and adapts the wetting boundary condition to model the contact angle. The pseudopotential model is widely used for various complex flow simulations due to its simplicity. To simulate the wetting phenomenon within this model, the mesoscopic interaction force between the boundary fluid and solid nodes is used to mimic the microscopic adhesive force between the fluid and the solid wall, and the bounce-back (BB) method is normally adopted to achieve the no-slip boundary condition. In this paper, the pseudopotential interaction forces are computed with eighth-order isotropy since fourth-order isotropy leads to the condensation of the dissolved component on curved walls. Due to the staircase approximation of curved walls in the BB method, the contact angle is sensitive to the shape of corners on curved walls. Furthermore, the staircase approximation makes the movement of the wetting droplet on curved walls not smooth. To solve this problem, the curved boundary method may be used, but due to the extrapolation process, most curved boundary conditions suffer from massive mass leakage when applied to the LB pseudopotential model. Through three test cases, it is found that the improved PSM scheme is mass conservative, that nearly identical static contact angles are observed on flat and curved walls under the same wetting condition, and that the movement of a wetting droplet on curved and inclined walls is smoother compared to the usual BB method. The present method is expected to be a promising tool for modeling flows in porous media and in microfluidic channels.

I. INTRODUCTION

After three decades of development, the lattice Boltzmann (LB) method has become an efficient and powerful tool to simulate fluid flows [1–4]. The LB method is widely used in simulating multicomponent (MC) flows [5]. Currently, there exist four categories of MC models: the free-energy model [6–8], the color-gradient model [9–12], the phase-field model [13–15], and the pseudopotential model [16, 17]. Among these models, the pseudopotential model shows a great advantage due to the simplicity of implementation. In the pseudopotential model, the mesoscopic interactions of pseudopotentials (based on component densities) are used to represent the microscopic intermolecular interactions and the separation of different components is a result of the mesoscopic repulsions.

One popular topic in the LB method is fluid-structure boundary conditions. The bounce-back (BB) method [18–20] is certainly the simplest and oldest boundary condition method. This method is exactly mass-conserving, and it leads to second-order accuracy when it is applied to a flat wall. However, this method suffers from accuracy issues when the wall geometry is complex since it uses a staircase to approximate curved walls. To overcome this problem, several curved boundary condition methods have been proposed. Based on the BB method, Noble and Torczynski [21] proposed the partially saturated method (PSM). They modified the collision operators based on the coverage of the fluid and the solid at the boundary nodes. This method is also exactly mass-conserving. Compared to the BB method, it makes the motion of fluid with complex boundary shapes smoother [22]. This method is more efficient when dealing with rest walls. While for moving walls, it is difficult to update the solid fractions of the boundary nodes at each time step. Bouzidi et al. [23] developed the interpolated bounce-back (IBB) method to improve the BB method. Their idea is to use linear or quadratic interpolation to correct the BB process according to the location of the wall. Their method can reach second-order accuracy for complex boundaries. But it may cause problems when the boundary is too narrow since there are not enough fluid nodes to do the interpolation. Furthermore, because of the interpolation process, the total mass in the system is not conserved [24]. Another group of curved boundary methods can be categorized as the ghost method [25–28]. The idea of the ghost method is to extrapolate the fluid property at boundary fluid nodes to virtual solid nodes at the boundary. The ghost methods are good at handling complex rest boundaries if they are properly applied. For moving boundaries, it is difficult to detect the position of the boundary at each time step. Besides, due to the extrapolation process, most of the ghost methods violate mass conservation.

The study of wetting phenomena is another popular topic in the LB method. Based on the BB method and the pseudopotential model, several wetting boundary methods were proposed to simulate the contact angle. Martys and Chen [29] first used the interaction force between fluid and adjacent solid nodes to mimic the adhesive force between the fluid and the wall. By adjusting

* Corresponding author: gang.WANG@univ-amu.fr

the fluid-solid interaction strength, different contact angles can be obtained. Benzi et al. [30] developed the virtual density method. They gave a constant virtual density to the wall so that they can use two free parameters to adjust contact angles. According to Young's equation [31], Huang et al. [32] developed an equation to approximate the contact angle using only interaction strength and equilibrium densities. Huang et al. [33] also simplified the virtual density scheme to have just one free parameter. The solid-fluid interaction strength is exactly the same as the fluid-fluid interaction strength, and one can change the contact angle by adjusting the virtual wall density. Different from previous methods, Li et al. [34] proposed a method in which the virtual wall density is not constant for the whole solid region, but has the same value as the local fluid density. In their method, since the virtual wall density is close to the local boundary fluid density, the fluid-solid and the fluid-fluid interactions are more consistent.

In this paper, we aim to extend the partially saturated method (PSM) to the LB pseudopotential MC model and adapt the wetting boundary condition to model the contact angle. The fluid-fluid and the fluid-solid interactions are computed with eighth-order isotropy since fourth-order isotropy leads to the condensation of the dissolved component on curved walls. The LB pseudopotential model is widely applied to simulate the flows in porous media and microfluidic channels where the flow behavior is dominated by wetting phenomena [35–37]. Currently, most wetting boundary condition schemes [29, 30, 32, 34] are based on the BB method due to its mass-conserving nature and simplicity. However, the staircase approximation of the BB method is not accurate enough to simulate the curved or complex walls of porous media and microfluidic channels [36–38]. One solution to this problem is to use a curved boundary condition. But most of the aforementioned curved boundary methods suffer from massive mass leakage when they are applied to the LB pseudopotential model since the extrapolation or the interpolation processes violate mass conservation [39]. Hence, in this paper, we choose the partially saturated method (PSM) which is a mass-conserving curved boundary method. The rest of this article is organized as follows. In Sec. II, we first review the original LB pseudopotential MC model and then introduce our improved PSM for the pseudopotential MC model. In Sec. III, we conduct three test cases to compare the performance of our improved PSM method and the wetting boundary condition based on the BB scheme. Finally, the conclusion and perspective are given in Sec. IV.

II. NUMERICAL MODEL

A. The LB pseudopotential MC model

Among the LB-based MC models, the pseudopotential MC model proposed by Shan and Chen [16, 17] is frequently used due to its simplicity. In the pseudopotential MC model, a repulsive force is introduced between components to create the separation of different components. There can be an arbitrary number (more than 1) of components. In this article, we only focus on the study of the two-component model, and the two components are represented by the red (r) and blue (b) colors. The distribution function for each component σ is given by the following discrete Boltzmann equation:

$$f_i^{(\sigma)}(\boldsymbol{x}+\boldsymbol{c}_i\Delta t, t+\Delta t) = f_i^{(\sigma)}(\boldsymbol{x},t)+\Omega_i^{(\sigma)}\Delta t+S_i^{(\sigma)}\Delta t \quad (1)$$

where $\Omega_i^{(\sigma)}$ is the Bhatnagar-Gross-Krook (BGK) collision operator given by:

$$\Omega_i^{(\sigma)} = -\frac{f_i^{(\sigma)}(\boldsymbol{x},t) - f_i^{eq(\sigma)}(\boldsymbol{x},t)}{\tau^{(\sigma)}} \quad (2)$$

where $\tau^{(\sigma)}$ is the relaxation time for the fluid σ. Throughout this article, $\tau^{(\sigma)} = 1$. The kinematic viscosity of the fluid σ is dependant on $\tau^{(\sigma)}$ by $\nu^{(\sigma)} = (\tau^{(\sigma)} - 0.5)/3 = 1/6$. $f_i^{eq(\sigma)}(\boldsymbol{x},t)$ is the equilibrium distribution function defined by:

$$f_i^{eq(\sigma)}(\boldsymbol{x},t) = \rho^{(\sigma)}\omega_i\left(1+\frac{\boldsymbol{c}_i\cdot\boldsymbol{u}}{c_s^2}+\frac{(\boldsymbol{c}_i\cdot\boldsymbol{u})^2}{2c_s^4}-\frac{\boldsymbol{u}\cdot\boldsymbol{u}}{2c_s^2}\right) \quad (3)$$

where discrete weights ω_i depend on velocity sets. In this article, D2Q9 and D3Q19 are used respectively for 2D and 3D simulations [40]. The speed of sound $c_s = 1/\sqrt{3}$. The fluid density for the component σ, the total fluid density and velocity are defined by:

$$\rho^{(\sigma)} = \sum_i f_i^{(\sigma)}(\boldsymbol{x},t),\ \rho = \sum_\sigma \rho^{(\sigma)} \quad (4)$$

and

$$\boldsymbol{u} = \frac{1}{\rho}\sum_\sigma\left(\sum_i f_i^{(\sigma)}\boldsymbol{c}_i + \frac{\boldsymbol{F}_{tot}^{(\sigma)}\Delta t}{2}\right). \quad (5)$$

The source term $S_i^{(\sigma)}$ is calculated by Guo forcing scheme [41]:

$$S_i^{(\sigma)} = \omega_i\left(1-\frac{\Delta t}{2\tau^{(\sigma)}}\right)\left(\frac{\boldsymbol{c}_i-\boldsymbol{u}}{c_s^2}+\frac{(\boldsymbol{c}_i\cdot\boldsymbol{u})\boldsymbol{c}_i}{c_s^4}\right)\boldsymbol{F}_{tot}^{(\sigma)}. \quad (6)$$

The total force on the σ component $\boldsymbol{F}_{tot}^{(\sigma)}$ is composed of three parts. They are respectively the gravitational force $\boldsymbol{F}_g^{(\sigma)}$, the intermolecular interaction force $\boldsymbol{F}_{int}^{(\sigma)}$, and the solid-fluid interaction force $\boldsymbol{F}_s^{(\sigma)}$:

$$\boldsymbol{F}_{tot}^{(\sigma)} = \boldsymbol{F}_g^{(\sigma)} + \boldsymbol{F}_{int}^{(\sigma)} + \boldsymbol{F}_s^{(\sigma)} \quad (7)$$

where the gravitational force is given by:

$$\boldsymbol{F}_g^{(\sigma)} = \rho^{(\sigma)}\boldsymbol{g}. \quad (8)$$

In the pseudopotential model [16, 17], the repulsive interaction is applied between components at adjacent nodes:

$$\boldsymbol{F}_{int}^{(\sigma)}(\boldsymbol{x}) = -\psi^{(\sigma)}(\boldsymbol{x}) G_{\sigma\tilde{\sigma}} \sum_i \omega_i \psi^{(\tilde{\sigma})}(\boldsymbol{x} + \boldsymbol{c}_i \Delta t) \boldsymbol{c}_i \Delta t \quad (9)$$

where $\psi^{(\sigma)}(\boldsymbol{x})$ is the pseudopotential of the component σ, and $G_{\sigma\tilde{\sigma}}$ is the interaction strength between two components. In this study, $\psi^{(\sigma)}(\boldsymbol{x}) = \rho^{(\sigma)}(\boldsymbol{x})$, and $G_{\sigma\tilde{\sigma}} = 4.5$.

To simulate the interaction between the solid wall and fluid components, the no-slip boundary condition and the wetting condition are required. The no-slip boundary condition can be realized by the BB scheme [18–20]. For the wetting condition, the adhesive force between fluid nodes and their adjacent solid nodes should be considered. Martys and Chen [29] developed a simple method to simulate this adhesion:

$$\boldsymbol{F}_{s}^{(\sigma)}(\boldsymbol{x}) = -G_{\sigma s} \rho^{(\sigma)}(\boldsymbol{x}) \sum_i \omega_i s(\boldsymbol{x} + \boldsymbol{c}_i \Delta t) \boldsymbol{c}_i \Delta t \quad (10)$$

where $s(\boldsymbol{x} + \boldsymbol{c}_i \Delta t)$ is a switch function. Its value is 1 for solid nodes and 0 for fluid nodes. $G_{\sigma s}$ is the adhesive strength between the fluid and the wall. Different contact angles can be obtained by tuning $G_{\sigma s}$.

Benzi et al. [30] proposed a virtual density scheme by adding a virtual solid density to Eq. (10):

$$\boldsymbol{F}_{s}^{(\sigma)}(\boldsymbol{x}) = -G_{\sigma s} \rho^{(\sigma)}(\boldsymbol{x}) \sum_i \omega_i s(\boldsymbol{x} + \boldsymbol{c}_i \Delta t) \rho^{s(\sigma)} \boldsymbol{c}_i \Delta t \quad (11)$$

where $\rho^{s(\sigma)}$ is the virtual solid density for the component σ, which is a constant value. One can change both $G_{\sigma s}$ and $\rho^{s(\sigma)}$ to adjust contact angles. Huang et al. [33] simplified the virtual density scheme by setting $G_{\sigma s} = G_{\sigma\tilde{\sigma}}$. The contact angle is only controlled by $\rho^{s(\sigma)}$. In the rest of this study, the virtual solid density scheme simplified by Huang et al. [33] is used.

Originally, discrete weights ω_i used in calculation of $\boldsymbol{F}_{int}^{(\sigma)}$ and $\boldsymbol{F}_{s}^{(\sigma)}$ are the same as that in Eq. (3), and it retains fourth-order isotropy of the interactions. To reduce spurious currents and increase the stability of the system, the calculation of the interactions can easily be extended to eighth-order isotropy by including the interactions with next-nearest fluid neighbors [42, 43]. At the walls, next-nearest virtual solid neighbors are also required to apply the virtual density scheme with eighth-order isotropy.

B. An improved PSM scheme for the LB pseudopotential MC model

The BB method [18–20] is a widely used boundary condition method because of its locality, efficiency, and simplicity. However, when it is applied to complex simulation geometries, it has an accuracy problem since it uses a staircase to approximate curved walls. Thus, Noble and Torczynski [21] proposed the partially saturated method (PSM) to solve this problem. In the PSM, a lattice boundary cell can be considered as pure solid, pure liquid, or a mixture of the solid and the fluid (partially saturated). The solid fraction depends on the solid coverage of a cell. The LB distribution function for the component σ is modified as:

$$\begin{aligned} f_i^{(\sigma)}(\boldsymbol{x} + \boldsymbol{c}_i \Delta t, t + \Delta t) =& f_i^{(\sigma)}(\boldsymbol{x}, t) + (1 - B^{(\sigma)}) \Omega_i^{f(\sigma)} \Delta t \\ &+ B^{(\sigma)} \Omega_i^{s(\sigma)} \Delta t \\ &+ (1 - B^{(\sigma)}) S_i^{(\sigma)} \Delta t \end{aligned} \quad (12)$$

where $\Omega_i^{f(\sigma)}$ is the standard collision operator for fluid nodes, and it has the same form as Eq. (2). The collision operator for solid nodes is $\Omega_i^{s(\sigma)}$, which can be written in the following way:

$$\begin{aligned} \Omega_i^{s(\sigma)} =& (f_{\bar{i}}^{(\sigma)}(\boldsymbol{x}, t) - f_{\bar{i}}^{eq(\sigma)}(\rho^{(\sigma)}, \boldsymbol{u})) \\ &- (f_i^{(\sigma)}(\boldsymbol{x}, t) - f_i^{eq(\sigma)}(\rho^{(\sigma)}, \boldsymbol{u}_s)) \end{aligned} \quad (13)$$

where $\bar{i}$ is the opposite direction of i. $\boldsymbol{u}$ is the local fluid velocity, and it is calculated the same way as Eq. (5). At pure solid nodes, $\boldsymbol{u} = \boldsymbol{u}_s$ where $\boldsymbol{u}_s$ is the velocity of the solid boundary. In this study, since walls are static, $\boldsymbol{u}_s = 0$.

The solid weight $B^{(\sigma)}$ is dependant on the solid fraction ϵ and the relaxation time $\tau^{(\sigma)}$:

$$B^{(\sigma)}(\boldsymbol{x}) = \frac{\epsilon(\boldsymbol{x})(\tau^{(\sigma)} - 0.5)}{(1 - \epsilon(\boldsymbol{x})) + (\tau^{(\sigma)} - 0.5)} \quad (14)$$

where the solid fraction ϵ value varies between 0 and 1.

The calculation of gravitational force does not change. The pseudopotential interaction force is modified to include the fluid-fluid interaction at partially saturated nodes:

$$\begin{aligned} \boldsymbol{F}_{int}^{(\sigma)}(\boldsymbol{x}) =& -\rho^{(\sigma)}(\boldsymbol{x}) \sum_{\tilde{\sigma}} G_{\sigma\tilde{\sigma}} \sum_i \omega_i (1 - \epsilon(\boldsymbol{x} + \boldsymbol{c}_i \Delta t)) \\ &\times \rho^{(\tilde{\sigma})}(\boldsymbol{x} + \boldsymbol{c}_i \Delta t) \boldsymbol{c}_i \Delta t. \end{aligned} \quad (15)$$

The solid-fluid interaction force is proposed as:

$$\boldsymbol{F}_s^{(\sigma)}(\boldsymbol{x}) = \begin{cases} -\rho^{(\sigma)}(\boldsymbol{x}) G_{\sigma\tilde{\sigma}} \sum_i \omega_i n^{(\tilde{\sigma})} \epsilon(\boldsymbol{x}+\boldsymbol{c}_i\Delta t)\rho(\boldsymbol{x}+\boldsymbol{c}_i\Delta t)\boldsymbol{c}_i\Delta t & \text{if } 0 < \epsilon(\boldsymbol{x}+\boldsymbol{c}_i\Delta t) < 1 \\ -\rho^{(\sigma)}(\boldsymbol{x}) G_{\sigma\tilde{\sigma}} \sum_i \omega_i n^{(\tilde{\sigma})} \epsilon(\boldsymbol{x}+\boldsymbol{c}_i\Delta t)\rho^s\boldsymbol{c}_i\Delta t & \text{if } \epsilon(\boldsymbol{x}+\boldsymbol{c}_i\Delta t) = 1 \end{cases} \tag{16}$$

where both partially and pure solid walls interact with the fluid. The partially solid density is approximated by the multiplication of the local fluid density and the local solid fraction: $\epsilon(\boldsymbol{x})\rho(\boldsymbol{x})$. The pure solid density ρ^s has a constant value and depends on the average fluid density at the boundary. The solid density consists of σ and $\tilde{\sigma}$ parts. $n^{(\sigma)}$ is the proportion of the solid density for the σ part. $n^{(\sigma)}$ is between 0 and 1, and the summation of two proportions is 1:

$$\sum_\sigma n^{(\sigma)} = 1. \tag{17}$$

In practice, after giving a value to the pure solid density ρ^s, one can tune the proportion parameter $n^{(r)} = 1 - n^{(b)}$ to generate the desired contact angle. For example, when $n^{(r)} = 1$ and $n^{(b)} = 0$, the wall is completely wetting for the r component; When $n^{(r)} = n^{(b)} = 0.5$, the contact angle is approximately 90°; When $n^{(r)} = 0$ and $n^{(b)} = 1$, the wall is completely non-wetting for the r component. According to Young's equation [31] and inspired by Huang et al. [32], the obtained contact angle θ_c can be approximated by:

$$cos(\theta_c) \approx n^{(r)} - n^{(b)}. \tag{18}$$

III. NUMERICAL RESULTS AND DISCUSSION

In this section, three test cases are conducted to compare the performance of the BB virtual density and the improved PSM schemes. For the improved PSM scheme, the solid fraction at curved boundary nodes is calculated by the cell decomposition method [44]. The wetting boundary conditions are chosen according to 11 groups of values given in Table I. For the BB virtual density scheme, we use the same wetting condition according to this table since the improved PSM scheme reduces to the BB virtual density scheme developed by Huang et al. [33] by setting $\epsilon(\boldsymbol{x}) = 1$ for $\epsilon(\boldsymbol{x}) > 0.5$, and $\epsilon(\boldsymbol{x}) = 0$ for $\epsilon(\boldsymbol{x}) \leq 0.5$. In the following test cases, we only specify the value of $n^{(r)}$ for simplicity, but the value of $n^{(b)}$ and ρ^s are also the same as in Table I.

TABLE I: Different wetting conditions according to different values of $n^{(r)}$, $n^{(b)}$ and ρ^s.

$n^{(r)}$	0	0.1	0.2	0.3	0.4	0.5	0.6	0.7	0.8	0.9	1
$n^{(b)}$	1	0.9	0.8	0.7	0.6	0.5	0.4	0.3	0.2	0.1	0
ρ^s	1.05	0.8	0.7	0.68	0.66	0.65	0.66	0.68	0.7	0.8	1.05

A. 2D case: static contact angles

Here we test the ability of the improved PSM and the BB virtual density wetting boundary condition methods to generate the desired contact angle on flat and curved walls. We first generate droplets on a flat wall and on the inner wall of a circular semicylinder, which is a concavely curved wall. The lattice system is chosen as $Nx \times Ny = 300 \times 150$ (in lattice unit). The radius and the location of the center of the semicylinder are respectively $145\Delta x$ and $(150.5\Delta x, 150\Delta x)$. Initially, two droplets with the same radius $R = 30\Delta x$ are placed on the flat and the concavely curved walls respectively. The centers of droplets (x_i, y_i) are respectively $(150.5\Delta x, 33\Delta x)$ and $(150.5\Delta x, 120\Delta x)$. Figure 1 shows the initialization of the droplets on the flat and the concavely curved walls with (a) the BB virtual density scheme and (b) the improved PSM scheme. The eighth-order scheme gives the same figure as the fourth-order scheme. The initial fluid densities at position (x, y) are given by:

$$\begin{cases} \rho^{(r)}(x,y) = 1,\ \rho^{(b)}(x,y) = 0.005 & \text{if } (x-x_i)^2 + (y-y_i)^2 \leq R \\ \rho^{(r)}(x,y) = 0.005,\ \rho^{(b)}(x,y) = 1 & \text{otherwise.} \end{cases} \tag{19}$$

Figure 2 shows the contact angles obtained on the flat and the concavely cylindrical walls at $t = 9 \times 10^4 \Delta t$. The BB virtual density scheme with fourth-order and eighth-order isotropy and the improved PSM scheme with eighth-order isotropy are applied. To measure the contact angle, we first apply the marching squares algorithm to find the droplet interface. Then, due to the symmetry of the system, we randomly select two points on the droplet interface to find the fitted circle. Finally, we find the intersection of the fitted circle with the wall and calculate the contact angle. Each contact angle is measured three times (each time different random interface points are selected to find the fitted circle), and the average value is given in this article. The maximum difference between the three measurements is 0.3° for both eighth-order schemes and 1.5° for the fourth-order BB virtual

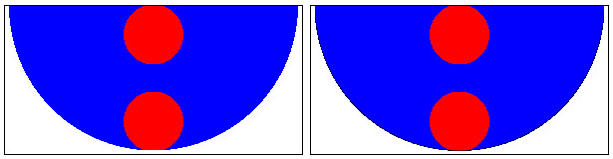

(a) BB (b) PSM

FIG. 1: The initialization of the droplets on the flat and the concavely curved walls. The red and blue colors represent the r and b components, respectively.

density scheme. It is shown in Fig. 2 that both schemes can be used to achieve different contact angles by tuning wetting boundary parameters. However, there is a condensation problem with the fourth-order BB virtual density scheme. As shown in Fig. 2(c), due to the condensation of the dissolved red fluid, two small droplets appear at the lower left and lower right parts of the cylinder wall. There is also the same condensation problem with the fourth-order improved PSM scheme (the figure is not presented here). Meanwhile, no condensation problem is observed for the BB virtual density and the improved PSM schemes with eighth-order isotropy (Figs. 2(f) and 2(i)). Besides, as shown in Fig. 2(c), the contact angle on the flat wall is 8.3° larger than that on the concavely curved wall when the fourth-order BB virtual density scheme is applied. In contrast, when we switch to eighth-order isotropy, the contact angles on the flat and the concave walls are more consistent with both the BB virtual density and the improved PSM schemes.

We also generate droplets on the outer wall of a cylinder, which is a convexly curved wall. The lattice system is chosen as $Nx \times Ny = 300 \times 300$ (in lattice unit). The periodic boundary condition is applied in all directions. The radius and the location of the center of the cylinder are respectively $75\Delta x$ and $(150.5\Delta x, 101\Delta x)$. The radius of the droplet is $50\Delta x$, and the center of the droplet is $(150.5\Delta x, 221\Delta x)$. The fluid densities are $\rho^{(r)} = 1$ and $\rho^{(b)} = 0.005$ inside the droplet and the opposite densities for the outside of the droplet. The initialization of the droplet on the convexly curved wall with the BB virtual density scheme and the improved PSM scheme are presented in Fig. 3(a) and Fig. 3(b), respectively.

Figure 4 presents the contact angles obtained on the convexly cylindrical wall with the fourth-order BB virtual density and the eighth-order improved PSM schemes at $t = 9 \times 10^4 \Delta t$. As the eighth-order BB scheme gives pictures very close to the eighth-order improved PSM method, it has not been presented. Figure 4(c) shows the condensation of a small droplet on the bottom of the cylinder wall when fourth-order isotropy is used to compute the interactions. On the contrary, there is no condensation problem with the eighth-order isotropy case. The contact angles achieved by the fourth-order BB virtual density scheme on the convexly curved wall are not consistent with the contact angles on the flat and the concavely curved walls (Fig. 2) under the same wetting condition. While for the eighth-order improved PSM scheme, contact angles are consistent for all three kinds of walls.

To compare the consistency of the contact angles on the flat and the curved walls by using the BB virtual density with both fourth-order and eighth-order and the improved PSM schemes with eighth-order isotropy, all 11 groups of wetting boundary condition parameters in Table I are applied to generate contact angles on the flat, the concavely curved, and the convexly curved walls. All contact angles are measured after running the simulations for $9 \times 10^4 \Delta t$ time steps when the eighth-order schemes give the static contact angles. For the fourth-order BB virtual density scheme, the unphysical condensation droplets continue to grow after $9 \times 10^4 \Delta t$ time steps, and there is no static regime for the system. The numerical results and the predicted contact angles according to Eq. (18) are plotted in Fig. 5. Compared with the fourth-order BB virtual density scheme, the contact angles obtained with the eighth-order BB virtual density and the eighth-order improved PSM schemes have a better agreement with the predicted contact angles from Eq. (18). There is a relatively large inconsistency of the contact angles on the flat and the curved walls under the same wetting condition when the fourth-order BB virtual scheme is applied (Fig. 5(a)), and small inconsistency for the eighth-order BB virtual scheme (Fig. 5(b)). In contrast, with the eighth-order improved PSM scheme, the contact angles on the three different walls almost overlap (Fig. 5(c)). To better show the improvement of the improved PSM scheme over the BB virtual density scheme in terms of consistency of contact angles on different walls, we plot the maximum difference of contact angles on the flat, the concavely curved, and the convexly curved walls with respect to the wetting parameter $n^{(r)}$ (Fig. 5(d)). With the eighth-order improved PSM scheme, the maximum contact angle difference is smaller than 1° under all the wetting conditions. However, for most of the partially wetting cases, the maximum contact angle difference is between 2° and 4° with the eighth-order BB virtual density scheme, and between 10° and 14° with the fourth-order BB virtual density scheme. On average, the eighth-order improved PSM provides a maximum contact angle difference that is around twenty times smaller than the fourth-order BB virtual density scheme and around five times smaller than the eighth-order BB virtual density scheme when the wall is partially wetting. Since the computation of the interactions with the fourth-order isotropy leads to the condensation problem on the curved walls and the large inconsistency of the contact angles on different walls, we only use the eighth-order isotropy to compute the interactions for the following tests.

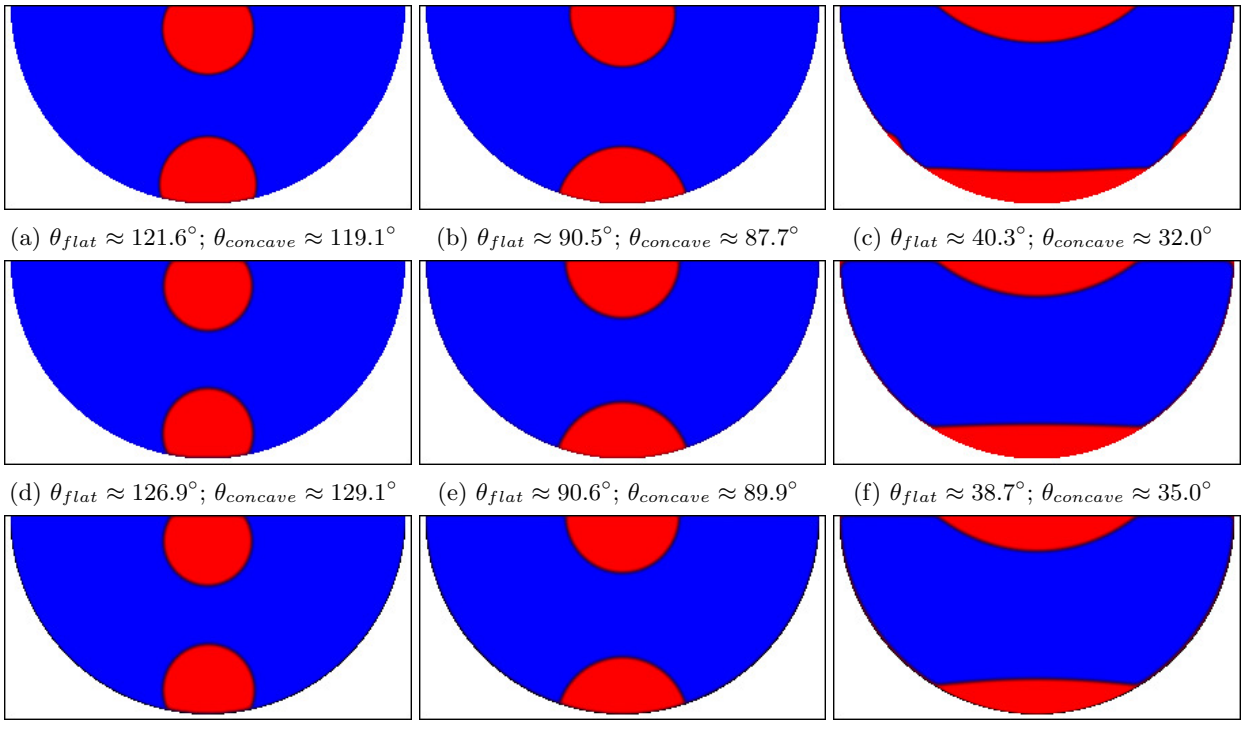

(a) $\theta_{flat} \approx 121.6^{\circ}$; $\theta_{concave} \approx 119.1^{\circ}$ (b) $\theta_{flat} \approx 90.5^{\circ}$; $\theta_{concave} \approx 87.7^{\circ}$ (c) $\theta_{flat} \approx 40.3^{\circ}$; $\theta_{concave} \approx 32.0^{\circ}$

(d) $\theta_{flat} \approx 126.9^{\circ}$; $\theta_{concave} \approx 129.1^{\circ}$ (e) $\theta_{flat} \approx 90.6^{\circ}$; $\theta_{concave} \approx 89.9^{\circ}$ (f) $\theta_{flat} \approx 38.7^{\circ}$; $\theta_{concave} \approx 35.0^{\circ}$

(g) $\theta_{flat} \approx 126.9^{\circ}$; $\theta_{concave} \approx 127.1^{\circ}$ (h) $\theta_{flat} \approx 90.6^{\circ}$; $\theta_{concave} \approx 90.7^{\circ}$ (i) $\theta_{flat} \approx 38.7^{\circ}$; $\theta_{concave} \approx 37.9^{\circ}$

FIG. 2: The contact angles on the flat and the concavely curved walls at $t = 9 \times 10^4 \Delta t$. The red and blue colors represent the r and b components, respectively. In (a), (b), and (c), the BB virtual density scheme with fourth-order isotropy of interactions is implemented with $n^{(r)} = 0.2, 0.5$, and 0.9, respectively. In (d), (e), and (f), the BB virtual density scheme with eighth-order isotropy is implemented with $n^{(r)} = 0.2, 0.5$, and 0.9, respectively. In (g), (h), and (i), the improved PSM scheme with eighth-order isotropy is applied with $n^{(r)} = 0.2, 0.5$, and 0.9, respectively.

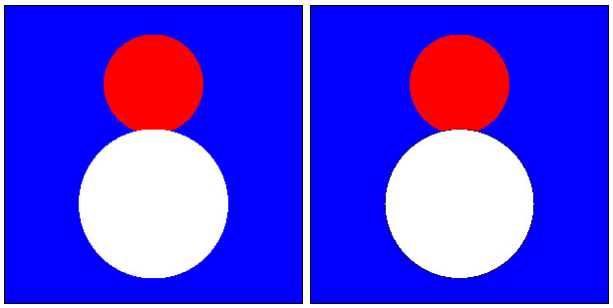

(a) BB (b) PSM

FIG. 3: The initialization of the droplet on the convexly curved wall. The red and blue colors represent the r and b components, respectively.

B. 2D case: a droplet sliding inside a rotating circular cylinder

This test is performed to study the influence of the curved wall on the movement of the wetting droplet when the BB virtual density and the improved PSM schemes with eighth-order isotropy are applied. To make the droplet rotate along the cylinder wall, a rotating gravity is applied to the droplet component instead of rotating the cylinder wall. The simulation box is $Nx \times Ny = 300 \times 300$ (in lattice unit). The radius and the location of the center of the cylinder are $145\Delta x$ and $(150.5\Delta x, 150.5\Delta x)$, respectively. Initially, a red droplet with the radius $30\Delta x$ and the center $(150.5\Delta x, 34\Delta x)$ is surrounded by the blue fluid. Inside the droplet, the fluid densities are $\rho^{(r)} = 1$ and $\rho^{(b)} = 0.005$, and the opposite densities for the outside of the droplet. The magnitude of the rotating gravity $\boldsymbol{g}$ is fixed to be 1×10^{-4} (in lattice unit) throughout the simulation. The direction of $\boldsymbol{g}$ is fixed at (0,-1) before $t = 1 \times 10^4 \Delta t$ to let the droplet relax, and then, from $t = 1 \times 10^4 \Delta t$ to $t = 5.2 \times 10^5 \Delta t$, gravity rotates in clockwise direction with the angular velocity $\omega_g = 2\pi/T$, where $T = 1.6 \times 10^5 \Delta t$ is the rotation period. After gravity rotates by a certain angle, the droplet starts to follow gravity and rotate on the wall. Figure 6 shows a partially wetting droplet ($n^{(r)} = 0.5$) on the inner cylinder wall under rotational gravity with the improved PSM scheme. To quantify the smoothness of droplet movement inside the cylinder, a droplet front point P is detected at each time step. P is defined as the intersection of the droplet interface with a circle (concentric with the cylinder) of radius 140 and it is computed by bicubic interpolation. In Fig. 6(a), gravity starts to

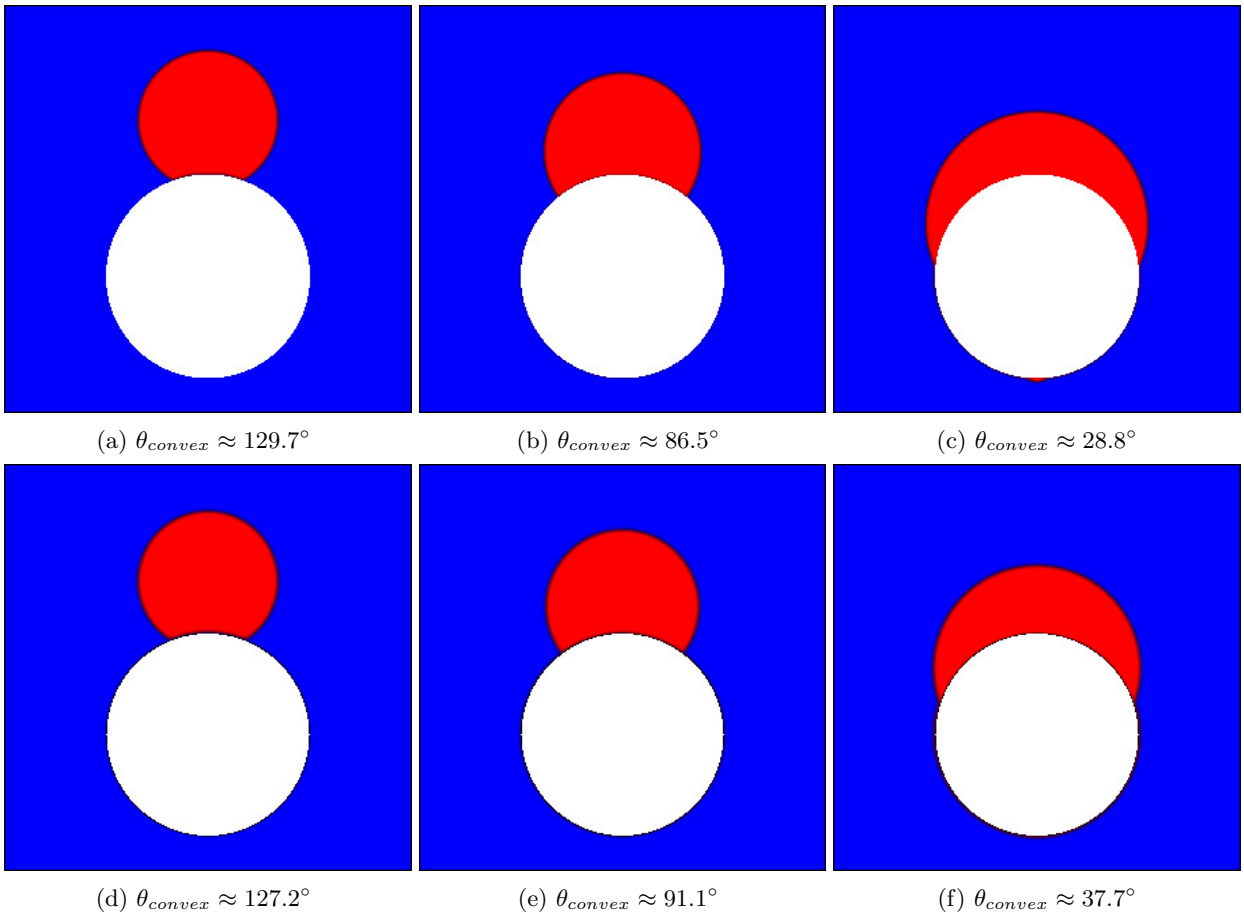

(a) $\theta_{convex} \approx 129.7°$ (b) $\theta_{convex} \approx 86.5°$ (c) $\theta_{convex} \approx 28.8°$

(d) $\theta_{convex} \approx 127.2°$ (e) $\theta_{convex} \approx 91.1°$ (f) $\theta_{convex} \approx 37.7°$

FIG. 4: The contact angles on the convexly curved wall at $t = 9 \times 10^4 \Delta t$. The red and blue colors represent the r and b components, respectively. In (a), (b), and (c), the fourth-order BB virtual density scheme is applied and the wetting parameter $n^{(r)}$ is respectively 0.2, 0.5, and 0.9. In (d), (e), and (f), the eighth-order improved PSM scheme is applied and the wetting parameter $n^{(r)}$ is respectively 0.2, 0.5, and 0.9.

rotate and the droplet is in the static state. Figure 6(b) shows the system after gravity has rotated for 90° and the droplet follows gravity with its rotation angle smaller than 90°.

Figure 7 shows the angular velocity ω_d $(rad/\Delta t)$ of the droplet front point P at the stationary regime for a quarter rotation period under the BB virtual density and the improved PSM schemes with eighth-order isotropy. The capillary number of the system is around 5.6×10^{-3}, and the Laplace number is around 330. To reach the stationary regime, we first let the droplet rotate for 2 perimeters, and then set t to 0 and start the measurement. As shown in Fig. 7(a), when the wall is non-wetting ($n^{(r)} = 0$) for the red fluid, the angular velocities of both the BB virtual density and the improved PSM schemes are smooth. Figures 7(b) and 7(c) show that the PSM angular velocities are smoother than the BB angular velocities under the partially wetting conditions, and the highest BB velocity variation is obtained for the $n^{(r)} = 0.5$ case. The mean relative error of the angular velocity ω_d (in the $n^{(r)} = 0.5$ case) is 21.4% for the eighth-order BB scheme and 5.1% for the eighth-order PSM scheme. The PSM scheme gives approximately four times smaller error than the BB scheme. When Ca is decreased to 2.8×10^{-3} ($T = 3.2 \times 10^5 \Delta t$), this error increases to 41.3% for the BB scheme and 11.0% for the PSM scheme. Both schemes perform worse, but the PSM error is still around four times smaller than the BB error. When the capillary number is increased to 1.1×10^{-2} ($T = 8.0 \times 10^4 \Delta t$), this error decreases to 5.2% for the BB scheme and 2.2% for the PSM scheme. Both schemes perform better. The PSM error is around 2.4 times smaller than the BB error, bringing it closer to the latter.

The droplet interface evolution at the stationary regime is shown in Fig. 8. The BB virtual density and the improved PSM schemes are applied. The droplet interface moves from the red line to the magenta line, and the time step difference between two adjacent interfaces is $1000\Delta t$. As shown in Figs. 8(d), 8(e), and 8(f), the droplet moves smoothly on the cylinder wall with the improved PSM scheme at all the wetting conditions. In contrast, for the BB virtual density scheme, droplet in-

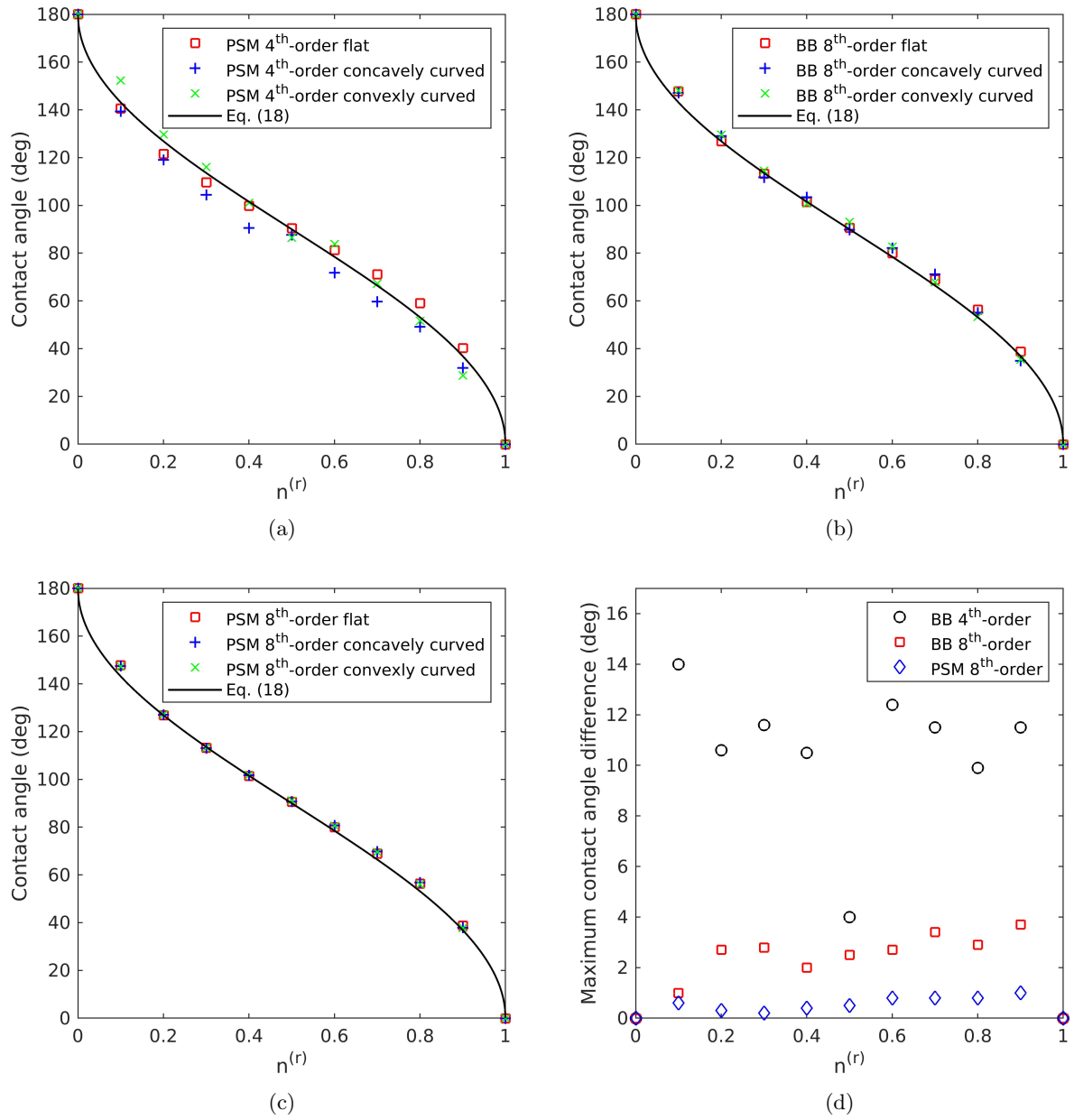

FIG. 5: (a)-(c) Contact angles w.r.t $n^{(r)}$ on the flat, the concavely curved, and the convexly curved surfaces with different schemes. (d) The maximum difference of contact angles on the flat, the concavely curved, and the convexly curved walls under the same wetting condition w.r.t the wetting parameter $n^{(r)}$.

terfaces are only equally spaced in the completely non-wetting case (Fig. 8(a)). As shown in Figs. 8(b) and 8(c), droplet interfaces are not equally spaced when the wall is partially wetting, especially in the $n^{(r)} = 0.5$ case. This is because in the BB partially wetting cases, the movement of the droplet is affected by the local corners on the staircase approximated wall. While in the BB non-wetting case, since the staircase wall is completely wet by the blue fluid, the corners of the wall are covered by the wetting fluid. Thus, it is equivalent that the droplet slides on the blue fluid instead of moving on the wall explaining why droplet interfaces are equally spaced.

C. 3D case: migrating of a droplet inside a square channel under gravity

In this test, we study the motion of a droplet inside a square channel under gravity. To investigate the influence of the inclination of the wall on the velocity of the droplet, the channel is placed with the wall respectively inclined (31°, 45° and 53°) and aligned (0°) with

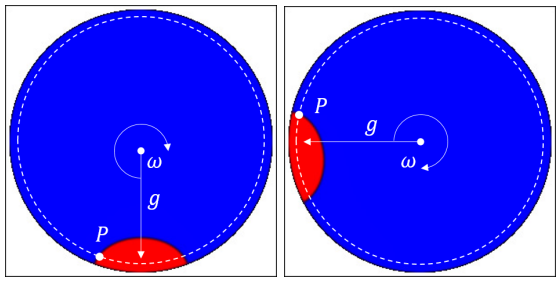

(a) $t = 1 \times 10^4 \Delta t$ (b) $t = 5 \times 10^4 \Delta t$

FIG. 6: The rotation of the droplet ($n^{(r)} = 0.5$) inside the circular cylinder under the effect of rotational gravity with the improved PSM scheme. The red and blue colors represent the r and b components, respectively.

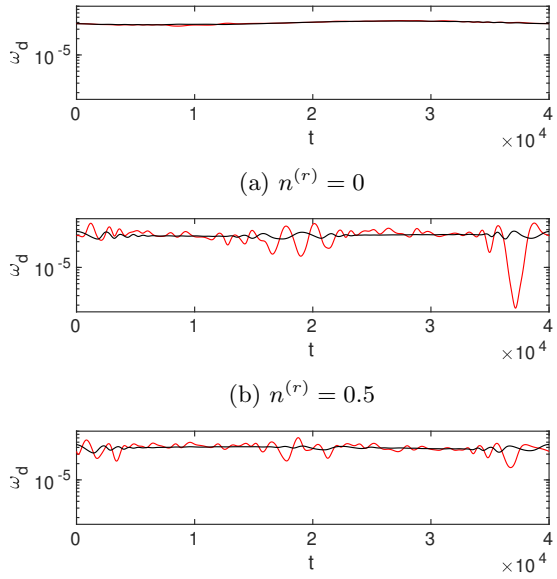

(a) $n^{(r)} = 0$

(b) $n^{(r)} = 0.5$

(c) $n^{(r)} = 0.8$

FIG. 7: The angular velocity ω_d ($rad/\Delta t$) of the droplet front point P at the stationary regime for a quarter rotation period under the eighth-order BB virtual density method (red line) and the eighth-order improved PSM method (black line). The capillary number of the system is around 5.6×10^{-3}, and the Laplace number is around 330.

the axis of the lattice. The aligned case is chosen as the reference since the PSM channel is equivalent to the BB channel when all channel walls are aligned with the axis of the lattice. If the inclined wall is smooth enough, the velocity of the droplet must not be affected by the inclination angle of the wall. The height and width of the channel are both $40\Delta x$, and the length of the channel is dependent on the inclination of the channel wall, but all the lengths approximate $233\Delta x$. Initially, a rectangular red droplet with a length of approximately $48\Delta x$ is introduced in the channel and is surrounded by the blue fluid. Inside the droplet, the fluid densities are $\rho^{(r)} = 1$ and $\rho^{(b)} = 0.005$, and the opposite densities for the outside of the droplet. The gravitational force $\boldsymbol{g}$ parallel to the channel walls and directed from left to right acts on the two fluids. The magnitude of gravity is 5.8×10^{-5} (in lattice unit). The contact angle of the droplet is obtained according to the values of parameters in Table I. Figure 9 presents a snapshot of the droplet ($n^{(r)} = 0.5$) inside a 31° inclined square channel at $t = 1.5 \times 10^4 \Delta t$. The periodic boundary condition is applied between the left and right boundaries, and also the top and bottom boundaries. The BB channel has a staircase approximation of the inclined wall (Fig. 9(a)), which appears to be less smooth than the PSM inclined wall (Fig. 9(b)).

A series of tests are performed to compare the average velocity (in lattice unit) of the droplet in channels with different wall inclination angles. The average velocity of the droplet at the stationary regime is measured (Fig. 10). As the droplet velocity changes under different wetting conditions, the capillary number of the system ranges from 3.6×10^{-3} to 4.7×10^{-3}. The Laplace number is around 220. The droplet velocities of the improved PSM scheme with eighth-order isotropy are almost unaffected by the wall inclination under the same wetting condition. The variation in the velocities is very small (smaller than 2%). However, for the BB virtual density scheme, the droplet velocities at different wall inclination angles are not consistent when the wall is partially wetting, especially when the wetting parameter $n^{(r)}$ is close to 0.5 where the contact angle is around 90°. The variation of the velocities reaches a maximum value of about 7% at $n^{(r)} = 0.5$. When $n^{(r)}$ increases from 0.5 to 0.9 or decreases from 0.5 to 0, the variation of the velocities becomes smaller but remains significant.

The evolution of the droplet interface in the $yz-$midplane at the stationary regime with $n^{(r)} = 0.5$ is plotted in Fig. 11 (see also supplementary Video 4 [45]). The droplet interface moves from the red line to the magenta line, and the time step difference between the two adjacent interfaces is $500\Delta t$. According to Figs. 11(e), 11(f), 11(g), and 11(h), the droplet interfaces are equally spaced at all inclination angles when the improved PSM scheme with eighth-order isotropy is used. For the BB virtual density method, the droplet moves smoothly on the 0° (Fig. 11(a)) and 45° (Fig. 11(c)) inclined walls. However, when the wall inclination is 31° (Fig. 11(b)) or 53° (Fig. 11(d)), the droplet interfaces are not equally spaced and asymmetrical with respect to the axis of the channel. This problem is mainly caused by the imbalance of the interaction force at the local corners of the inclined wall. In contrast, when the wall is 45° inclined, all the corners are the same, and when the wall is aligned, there is no corner on the wall. Similar to the previous test case, we find that when $n^{(r)}$ is closer to 0 or 1, the movement of the droplet becomes smoother with the BB virtual density scheme. This is because when the wall is closer to completely non-wetting or completely wetting,

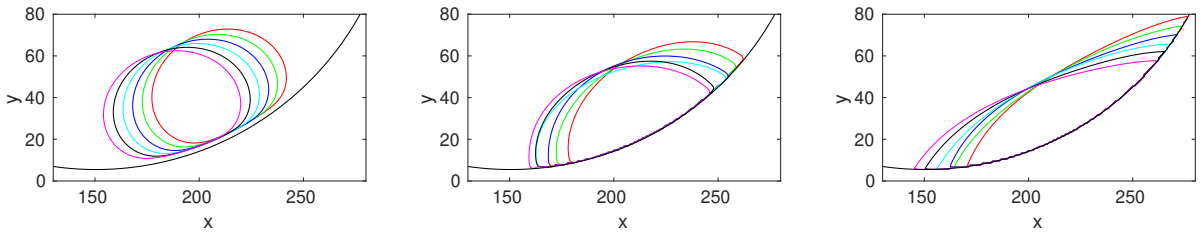

(a) 8^{th}-order BB; $n^{(r)} = 0$ (b) 8^{th}-order BB; $n^{(r)} = 0.5$ (c) 8^{th}-order BB; $n^{(r)} = 0.8$

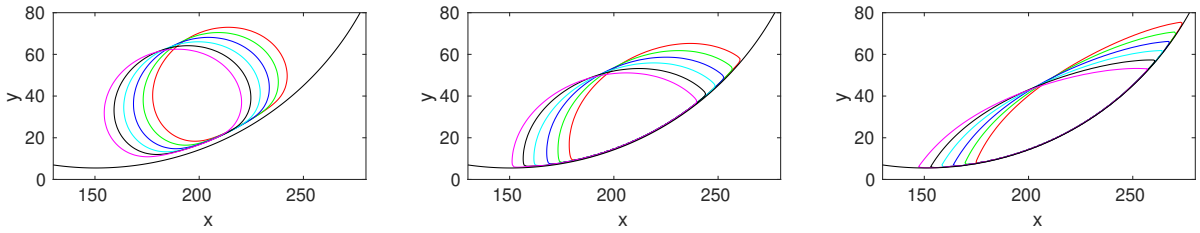

(d) 8^{th}-order PSM; $n^{(r)} = 0$ (e) 8^{th}-order PSM; $n^{(r)} = 0.5$ (f) 8^{th}-order PSM; $n^{(r)} = 0.8$

FIG. 8: The droplet interface evolution at the stationary regime (see supplementary Video 1, 2, and 3 [45]). The droplet interface moves from the red line to the magenta line, and the time step difference between two adjacent interfaces is $1000\Delta t$.

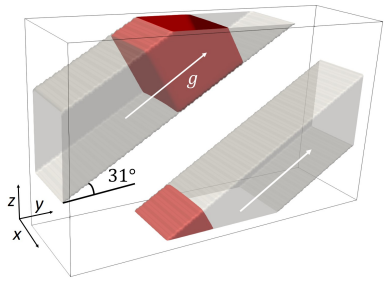

(a) 8^{th}-order BB

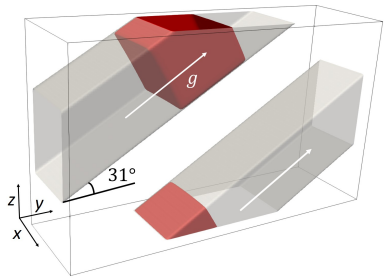

(b) 8^{th}-order PSM

FIG. 9: A snapshot of the droplet ($n^{(r)} = 0.5$) inside a 31° inclined square channel at $t = 1.5 \times 10^4 \Delta t$. The red color represents the r component.

the corners of the inclined wall are more covered by the wetting fluid. Thus, the non-wetting fluid tends to slide on a layer of the wetting fluid instead of moving on the wall.

IV. CONCLUSION AND PERSPECTIVE

In this work, we proposed an improved PSM scheme to simulate pseudopotential MC flows. This proposed scheme is fully mass-conserving so that the droplet size does not change while flowing. The pseudopotential interactions are computed with eighth-order isotropy since fourth-order isotropy leads to a condensation problem on the curved walls and a large inconsistency of the contact angles on the flat and the curved walls. It should be emphasized that eighth-order isotropic terms are only used to compute the pseudopotential interaction forces, so the increase in computation time is acceptable. It has been found that our method is capable of producing nearly identical contact angles on the flat, the concavely curved, and the convexly curved walls when the same wetting condition is applied, and the contact angles obtained in the simulations are in good agreement with Eq. (18) given according to Young's equation [31]. Whereas for the BB virtual density scheme, there is around a five times higher inconsistency of the contact angles on the different walls when the partially wetting boundary condition is applied. Furthermore, the improved PSM method reduces grid dependence of the moving contact line [46–49]. It is shown that with the improved PSM scheme, the droplet moves smoothly on the curved and inclined walls and the velocity of the droplet is almost not affected by the wall inclination angle with respect to the lattice under all wetting conditions. However, for the BB virtual density scheme, when the wall is partially wetting, the local corners on the curved and inclined walls affect the movement of the droplet. When the wetting condition of the wall is

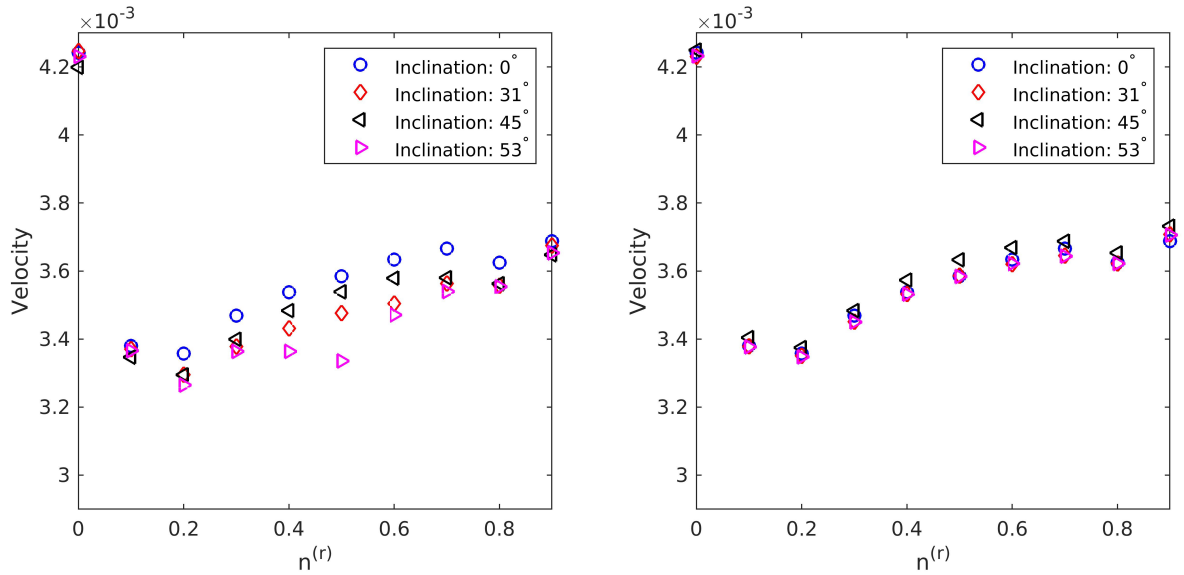

(a) 8^{th}-order BB (b) 8^{th}-order PSM

FIG. 10: The average velocity (in lattice unit) of the droplet w.r.t $n^{(r)}$ at different inclinations of the wall. As the droplet velocity changes under different wetting conditions, the capillary number of the system ranges from 3.6×10^{-3} to 4.7×10^{-3}. The Laplace number is around 220.

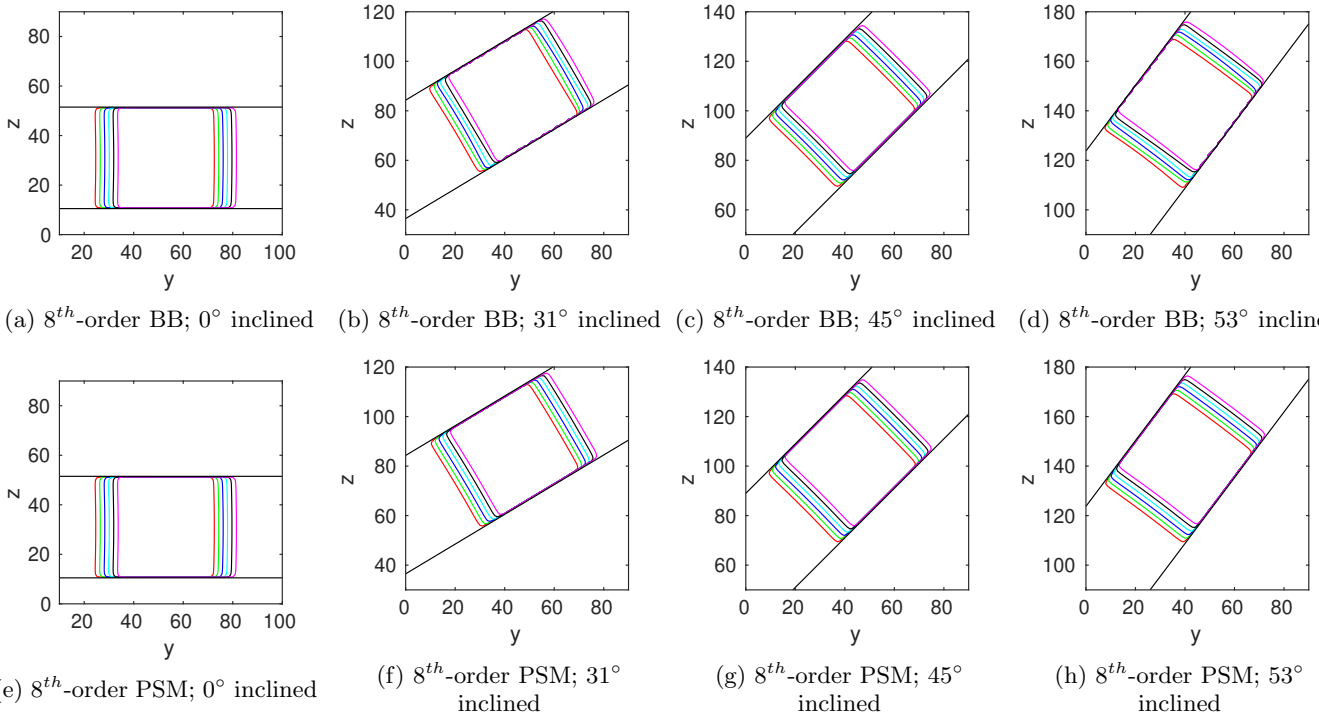

(a) 8^{th}-order BB; 0° inclined (b) 8^{th}-order BB; 31° inclined (c) 8^{th}-order BB; 45° inclined (d) 8^{th}-order BB; 53° inclined

(e) 8^{th}-order PSM; 0° inclined (f) 8^{th}-order PSM; 31° inclined (g) 8^{th}-order PSM; 45° inclined (h) 8^{th}-order PSM; 53° inclined

FIG. 11: The evolution of the droplet interface in the $yz-$midplane at the stationary regime with $n^{(r)} = 0.5$ (see supplementary Video 4 [45]). The droplet interface moves from the red line to the magenta line, and the time step difference between the two adjacent interfaces is $500\Delta t$.

closer to completely non-wetting or completely wetting, the movement of the droplet becomes smoother and the wall inclination angle has less influence on the droplet velocity since the corners on the staircase approximation

are covered with a layer of the wetting fluid, which increases the smoothness of the walls.

Overall, our improved PSM scheme is superior to the BB virtual density scheme in simulating pseudopotential MC flows with curved or complex wall geometries over a wide range of wetting boundary conditions. The present method appears to be a powerful tool for simulating MC flows in porous media and in microfluidic channels.

[1] T. Krüger, H. Kusumaatmaja, A. Kuzmin, O. Shardt, G. Silva, and E. M. Viggen, *The lattice Boltzmann method* (Springer, 2017).

[2] S. Chen and G. D. Doolen, *Ann. Rev. Fluid Mech.* **30**, 329 (1998).

[3] X. He, L. Luo, *Phys. Rev. E* **56**, 6811 (1997).

[4] M. Latva-Kokko and D. H. Rothman, *Phys. Rev. Lett* **98**, 254503 (2007).

[5] J. Zhang, *Microfluid. Nanofluidics* **10**, 1 (2011).

[6] W. R. Osborn, E. Orlandini, M. R. Swift, J. M. Yeomans, and J. R. Banavar, *Phys. Rev. Lett* **75**, 4031 (1995).

[7] M. R. Swift, E. Orlandini, W. R. Osborn, and J. M. Yeomans, *Phys. Rev. E* **54**, 5041 (1996).

[8] T. Inamuro, N. Konishi, and F. Ogino, *Comput. Phys. Commun.* **129**, 32 (2000).

[9] D. H. Rothman and J. M. Keller, *J. Stat. Phys.* **52**, 1119 (1988).

[10] A. K. Gunstensen, D. H. Rothman, S. Zaleski, and G. Zanetti. *Phys. Rev. A* **43**, 4320 (1991).

[11] D. Grunau, S. Chen, and K. Eggert, *Phys. Fluids A* **5**, 2557 (1993).

[12] U. D'Ortona, D. Salin, M. Cieplak, R. Rybka, and J. Banavar, *Phys. Rev. E* **51**, 3718 (1995).

[13] T. Lee and L. Liu, *J. Comput. Phys.* **229**, 8045 (2010).

[14] A. Fakhari and M. H. Rahimian, *Phys. Rev. E* **81**, 036707 (2010).

[15] Q. Li, K. H. Luo, Y. J. Gao, and Y. L. He, *Phys. Rev. E* **85**, 026704 (2012).

[16] X. Shan and H. Chen, *Phys. Rev. E* **47**, 1815 (1993).

[17] X. Shan and H. Chen, *Phys. Rev. E* **49**, 2941 (1994).

[18] I. Ginzbourg and P. M. Adler, *J. Phys. II* **4**, 191 (1994).

[19] A. J. C. Ladd, *J. Fluid Mech.* **271**, 285 (1994).

[20] X. He, Q. Zou, L. Luo, and M. Dembo, *J. Stat. Phys.* **87**, 115 (1997).

[21] D. R. Noble and J. R. Torczynski, *Int. J. Mod. Phys. C* **9**, 1189 (1998).

[22] O. E. Strack and B. K. Cook, *Int. J. Numer. Methods Fluids* **55**, 103 (2007).

[23] M. Bouzidi, M. Firadaouss, and P. Lallemand, *Phys. Fluids* **13**, 3452 2001.

[24] P. H. Kao and R. J. Yang, *J. Comput. Phys.* **227**, 5671 (2008).

[25] O. Filippova and D. Hänel, *J. Comput. Phys.* **147**, 219 (1998).

[26] R. Mei, L. Luo, and W. Shyy, *J. Comput. Phys.* **155**, 307 (1999).

[27] Z. Guo, C. Zheng, and B. Shi, *Phys. Fluids* **14**, 2007 (2002).

[28] A. Tiwari and S. P. Vanka, *Int. J. Numer. Methods Fluids* **69**, 481 (2012).

[29] N. S. Martys and H. Chen, *Phys. Rev. E* **53**, 743 (1996).

[30] R. Benzi, L. Biferale, M. Sbragaglia, S. Succi, and F. Toschi, *Phys. Rev. E* **74**, 021509 (2006).

[31] T. Young, *Philos. Trans. R. Soc. London* **95**, 65 (1805).

[32] H. Huang, D. T. Thorne, M. G. Schaap, and M. C. Sukop, *Phys. Rev. E* **76**, 066701 (2007).

[33] H. Huang, Z. Li, S. Liu, and X. Lu, *Int. J. Numer. Methods Fluids* **61**, 341 (2009).

[34] Q. Li, K. H. Luo, Q. J. Kang, and Q. Chen, *Phys. Rev. E* **90**, 053301 (2014).

[35] H. Liu, Q. Kang, C. R. Leonardi, S. Schmieschek, A. Narváez, B. D. Jones, J. R. Williams, A. J. Valocchi, and J. Harting, *Comput. Geosci.* **20**, 777 (2016).

[36] C. Pan, M. Hilpert, and C. T. Miller, *Water Resour. Res.* **40**, W01501 (2004).

[37] J. Du, N. Ibaseta, and P. Guichardon, *Chem. Eng. Res. Des.* **159**, 615 (2020).

[38] P. Zhu and L. Wang, *Lab Chip* **17**, 34 (2017).

[39] Y. Yu, Q. Li, and Z. X. Wen, *Comput. Fluids* **208**, 104638 (2020).

[40] Y. Qian, D. d'Humières, and P. Lallemand, *Europhys. Lett.* **17**, 479 (1992).

[41] Z.Guo, C. Zheng, and B. Shi, *Phys. Rev. E* **65**, 046308 (2002).

[42] X. Shan, *Phys. Rev. E* **73**, 047701 (2006).

[43] M. Sbragaglia, R. Benzi, L. Biferale, S. Succi, K. Sugiyama, and F. Toschi, *Phys. Rev. E* **75**, 026702 (2007).

[44] D. R. J. Owen, C. R. Leonardi, and Y. T. Feng, *Int. J. Numer. Methods Eng.* **87**, 66 (2011).

[45] See supplemental material at [href will be added by editor]. Video 1, 2, 3: the movement of a droplet inside the circular wall with $n^{(r)} = 0$, $n^{(r)} = 0.5$, and $n^{(r)} = 0.8$, respectively; Video 4: the movement of a droplet inside a 31° inclined channel with $n^{(r)} = 0.5$.

[46] Y. Sui, H. Ding, and P. D. M. Spelt, *Annu. Rev. Fluid Mech.* **46**, 97 (2014).

[47] J. B. Dupont and D. Legendre, *J. Comput. Phys.* **229**, 2453 (2010).

[48] S. Afkhami, S. Zaleski, and M. Bussmann, *J. Comput. Phys.* **228**, 5370 (2009).

[49] D. Legendre and M. Maglio, *Comput. Fluids* **113**, 2 (2015).